Chemical Science

ROYAL SOCIETY OF CHEMISTRY

EDGE ARTICLE

View Article Online
View Journal | View Issue

Cite this: *Chem. Sci.*, 2023, **14**, 9733

All publication charges for this article have been paid for by the Royal Society of Chemistry

A functional unit combination strategy for enhancing red room-temperature phosphorescence†

Shuaiqiang Zhao, Zhiqiang Yang, Xiangyu Zhang, Haichao Liu, * Yingbo Lv, Shiyin Wang, Zhongzhao Yang, Shi-Tong Zhang and Bing Yang *

Received 17th July 2023
Accepted 21st August 2023

DOI: 10.1039/d3sc03668e

rsc.li/chemical-science

Red room-temperature phosphorescence (RTP) materials based on non-metallic organic compounds are less reported compared to the commonly found green RTP materials. Here, we propose a novel approach to obtain red RTP materials by integrating and combining two functional units, resembling a jigsaw puzzle. In this approach, benzo[*c*][2,1,3]thiadiazole (BZT) serves as the red RTP unit, while a folding unit containing sulphur/oxygen is responsible for enhancing spin–orbit coupling (SOC) to accelerate the intersystem crossing (ISC) process. Three new molecules (SS-BZT, SO-BZT, and OO-BZT) were designed and synthesized, among which SS-BZT and SO-BZT with folded geometries demonstrate enhanced red RTP in their monodisperse films compared to the parent BZT. Meanwhile, the SS-BZT film shows a dual emission consisting of blue fluorescence and red RTP, with a significant spectral separation of approximately 150 nm, which makes the SS-BZT film highly suitable for applications in optical oxygen sensing and ratiometric detection. Within the oxygen concentration range of 0–1.31%, the SS-BZT film demonstrates a quenching constant of 2.66 kPa^{-1} and a quenching efficiency of 94.24%, indicating that this probe has the potential to accurately detect oxygen in a hypoxic environment.

Introduction

Purely organic room-temperature phosphorescence (RTP) materials have attracted tremendous interest in recent years, due to their unique triplet emission with long lifetime and environmental sensitivity. As a good alternative to metallic complexes,[1,2] they show various potential applications in organic light-emitting diodes (OLEDs),[3–6] bioimaging,[7–11] encryption and anti-counterfeiting.[12–16] The process of harvesting phosphorescence involves two main stages: one is the intersystem crossing (ISC) process from excited singlet states to excited triplet states, which determines the yield of triplet excitons; the other is the radiation of triplet excitons that competes with a series of non-radiative processes (*e.g.*, molecular thermal motion and collision).[17–19] Correspondingly, two effective measures have been taken to improve RTP efficiency: one is promoting the generation of triplet excitons through enhancing spin–orbit coupling (SOC) to accelerate the ISC process, which is generally realized by introducing heavy atoms (Br, I, Se),[20–27] heteroatoms (B, N, O, S),[28–31] aromatic carbonyl groups,[32–34] and folded configurations[35,36] in organic molecule frameworks; the other is to make triplet radiation more competitive by suppressing the non-radiative processes, such as molecular crystallization,[37–39] dispersion in a rigid polymer matrix,[40–44] and host–guest system.[45–50] Through unremitting efforts, a variety of purely organic RTP material systems have been explored with diverse application prospects. However, the reported RTP materials mainly focus on the blue–green or yellow–green color gamut, and rarely involve the red RTP,[51–58] which can be attributed to the limitation of energy gap law.[59] To broaden the range of material systems and explore more potential applications for RTP materials, it is worthwhile to dedicate further research and development to red RTP materials.

Benzo[*c*][2,1,3]thiadiazole (BZT) with two nitrogen atoms and one sulphur atom in a fused ring generally serves as an electron acceptor to construct donor–acceptor molecular backbones for improving luminescence properties, because of its electron-deficient characteristic.[60–65] However, as an independent emitter, the emission properties of BZT were scarcely systemically studied, especially for red RTP.[66–70] According to preliminary studies in our group, BZT showed weak blue fluorescence in its crystalline state. After being dispersed in polymethyl methacrylate (PMMA) to form an amorphous film, this film displayed a new emission band around 600 nm following the removal of oxygen, indicating the presence of RTP. While

State Key Laboratory of Supramolecular Structure and Materials, College of Chemistry, Jilin University, Changchun 130012, China. E-mail: hcliu@jlu.edu.cn; yangbing@jlu.edu.cn

† Electronic supplementary information (ESI) available: Synthetic details, theoretical calculations, photophysical measurements, and oxygen sensing. CCDC 2266086–2266088. For ESI and crystallographic data in CIF or other electronic format see DOI: https://doi.org/10.1039/d3sc03668e

faint red RTP emission was observed in BZT due to weak SOC, it has the potential to achieve enhanced red RTP emission through a rational molecular engineering design.

In our previous research, we have found that thianthrene (TA), which has a folded molecular geometry, displayed efficient yellow–green RTP based on a mechanism of folding-induced SOC enhancement.[35,36,71,72] The presence of lone-pair electrons on the sulphur atoms in TA plays a crucial role in this SOC enhancement. Herein, we propose a functional combination strategy by incorporating TA and BZT units into a single molecule. The aim of this strategy is leveraging the individual advantages of TA and BZT, making them complementary to each other, that is to say, TA is responsible for the folding-induced SOC enhancement while BZT acts as a red RTP emitter core, and the cooperation between them is expected to generate efficient red RTP emission. As a result, a constructed molecule, thianthreno[2,3-*c*][1,2,5]thiadiazole (SS-BZT), shows an improved efficiency of red RTP compared to isolated BZT when incorporated into polymer films; moreover, SS-BZT demonstrates a substantial spectral separation between fluorescence and RTP emissions. Both experimental and theoretical investigations demonstrate that this enhanced red RTP can be ascribed to the effective cooperation between the ISC process and triplet exciton radiation by the functional unit combination strategy. Furthermore, the SS-BZT-doped polymer film performs very well in low-concentration and even trace oxygen sensing and detection. At the same time, the counterparts phenoxathiino[2,3-*c*][1,2,5]thiadiazole (SO-BZT) and benzo[5′,6′][1,4]dioxino[2′,3′:4,5]benzo[1,2-*c*][1,2,5]thiadiazole (OO-BZT) were also designed and synthesized for a systematic comparison. As a whole, this work proposes a new functional unit combination strategy to design novel RTP materials, especially for red RTP emitters, and also provides a novel optical probe for ratiometric oxygen sensing and detection based on a single luminophore.

Results and discussion

Molecular design

A TA molecule with two sulphur atoms as joints bridging two benzene rings[73,74] shows a folded configuration in its ground state, which facilitates the folding-induced significant enhancement of SOC compared to the planar configuration.[35,36] In experiments, both the TA crystal and TA-doped PMMA film have been observed to produce efficient yellow–green and green RTP emission. Furthermore, the rational chemical modification based on the TA skeleton can effectively adjust the RTP properties to a certain extent towards red RTP emission as we desired. One interesting aspect of our observations is that the extended π-conjugation at the 2-position of TA enables us to tune the RTP emission color from green to yellow.[75] However, it is important to note that the further redshift of RTP emission is limited when it comes to extending the π-conjugation of TA. To further exploit the potential of TA in highly efficient and full-color gamut RTP materials, one effective approach is to graft the TA unit onto other RTP chromophores, which can allow for realization of tunable RTP properties over a broader range. By employing a strategy of functional unit combination, a new molecule can be developed that integrates both TA and BZT, in which each unit performs its own distinct function, namely, BZT serves as a red RTP emitter core while TA contributes to the generation of more triplet excitons through folding-induced SOC enhancement. To facilitate easy synthesis, a fused-ring connection mode is employed between two functional units, aiming to ensure not only the rigidity of the molecular structure to suppress the non-radiative process but also the desirable transition configuration of excited states (singlet and triplet) to accelerate the ISC process, which synergistically enhance red RTP emission compared to isolated BZT. As shown in Scheme 1 and Fig. S1,† the resultant SS-BZT molecule is designed with a one-dimensional linear fused ring structure. To gain a better understanding of the properties of SS-BZT, the counterparts of TA, phenoxathiine (PX) and dibenzo[*b*,*e*][1,4]dioxine (DX) are chosen and combined with BZT to form two analogues (SO-BZT and OO-BZT) for the purpose of comparison. These three compounds were synthesized through a ring-formed nucleophilic aromatic substitution reaction (Scheme S1†).

Structures and photophysical properties of crystals

Single crystals of the synthesized compounds, SS-BZT, SO-BZT, and OO-BZT, were grown to investigate their molecular geometries and molecular packing structures. The single crystal X-ray diffraction (SCXRD) experiment revealed that BZT and its derivatives in crystals were all stacked in a one-dimensional π–π aggregation mode with a small displacement along the long axis of given molecules, which are obviously different from dimeric stacking of TA in crystals (PX and DX crystals show irregular packing and one dimensional π–π stacking, respectively) (Fig. S2–S4†). Importantly, when an electron-donating TA unit is introduced, the folding geometry of the molecule is synchronously transplanted into SS-BZT, and the folding dihedral angle is 133.64°, which is slightly larger than the 126.88° of TA (Fig. 1). This increased folding dihedral angle observed in SS-BZT can be attributed to the extended π-conjugation of SS-BZT with enhanced electron delocalization, facilitating the planarization of molecular conformation. Similarly, the folding dihedral angle in SO-BZT is also observed to be enlarged, measuring 172.45°. However, in the case of OO-BZT, only a minor change in the folding dihedral angle is observed. The folding dihedral

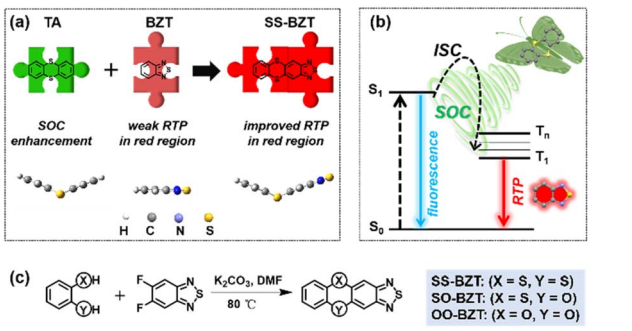

Scheme 1 (a) Molecular design strategy. (b) Schematic of folding-induced SOC enhancement and triplet state radiation for SS-BZT. (c) Synthesis routes to SS-BZT, SO-BZT, and OO-BZT.

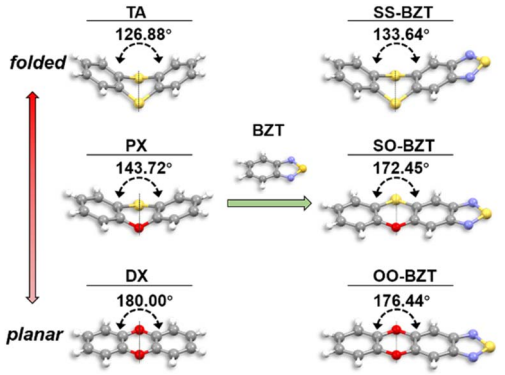

Fig. 1 Molecular geometries of TA, PX, DX, BZT, SS-BZT, SO-BZT, and OO-BZT obtained from their single crystals.

angle exhibits a gradual increase from SS-BZT to SO-BZT and OO-BZT, which is in line with the trend observed from TA to PX and DX.[36] These results indicate that these designed molecules have successfully inherited the folding geometry observed in TA and red RTP from BZT through the strategy of functional unit combination between BZT and folding units.

Photoluminescence (PL) spectra and time-resolved PL spectra of all the crystals were measured at room temperature (RT) under both air and vacuum conditions, as well as at 77 K (Fig. S5–S7†). At RT, both BZT and TA crystals show two distinct emission bands with a short lifetime in the short-wavelength region and a long lifetime in the long-wavelength region, which can be assigned to fluorescence and RTP. The SS-BZT crystal presents an emission band peaking at 530 nm and a tailing band with a long lifetime, corresponding to fluorescence and RTP, respectively. At a temperature of 77 K, the SS-BZT crystal exhibits two distinct emission bands in the range of 450–600 nm and 600–800 nm, which are also attributed to fluorescence and phosphorescence, respectively. Similar to SS-BZT, both SO-BZT and OO-BZT crystals also demonstrate a dual emission profile consisting of fluorescence and phosphorescence at a temperature of 77 K. Compared to parent BZT, red phosphorescence of these BZT derivatives at 77 K can be observed by the naked eyes even after the excitation light source has been removed.

As a matter of fact, the crystals of BZT and its derivatives show insufficient photoluminescence quantum yields (PLQYs) and almost invisible RTP due to the quenching effect of molecular aggregation (Fig. S2†). Hence, we further chose benzophenone (BPO) as the host material to disperse these compounds in order to investigate single molecule RTP properties.[76,77] To obtain the single molecule state, we optimized the doping ratios and successively prepared the doped crystals for BZT and its derivatives as the guests and BPO as the host, including 0.01 wt%, 0.05 wt%, 0.10 wt%, 0.20 wt%, 0.50 wt% and 1.00 wt%. Taking SS-BZT : BPO doped crystals for instance, as the doping ratios increase, these doped crystals exhibit a change in apparent color from being colorless to turning yellow when exposed to sunlight, as well as an emission color transformation from blue to reddish orange and eventually to orange yellow when irradiated under a UV (365 nm) lamp. Corresponding to their PL spectra, two distinct emission bands were observed, in which the emission band in the blue region is attributed to the host BPO while the long-lived emission band in the red region is assigned to the guest SS-BZT (Fig. 2a–c). With increasing doping ratios, the emission intensity of the host BPO in the blue region experiences a sharp decline, while the red RTP emission intensity of the guest SS-BZT displays a rapid increase, indicating an efficient energy transfer taking place from the host to the guest. Notably, when the doping ratio exceeds 0.20%, there is a slight increase in the emission intensity around 500 nm, which may be caused by the formation of SS-BZT aggregates. The formation of SS-BZT aggregates should be adverse to the phosphorescence quantum yields (Φ_Ps), and the recorded Φ_Ps for the SS-BZT : BPO doped crystals were 0.21%, 0.60%, 2.33%, 1.44%, 1.42%, and 1.64% as the doping ratio increases (Table S1†). Overall, the 0.10 wt% doped crystal exhibits the best performance. Therefore, when the doped ratio is below 0.20%, it is possible to achieve a fully single molecule state of SS-BZT. Compared to the single crystal of SS-BZT, the RTP emission of the doped crystals is significantly strengthened, so that the red RTP of doped crystals under UV irradiation can be directly observed by the naked eye. As for BZT and other BZT derivatives, with increasing doping ratios, the emission bands of the doped crystals also gradually enhance in the red region, but their respective maximum Φ_Ps are obviously inferior to those of SS-BZT : BPO doped crystals, especially for the BZT : BPO doped crystal. The detailed data are shown in Fig. S8–S11 and Table S1.†

Photophysical properties of solutions and films

To investigate the basic photophysical properties of SS-BZT and its counterparts, UV-vis absorption and PL spectra were recorded in four solvents with varying polarities (Fig. S12–S15†). For each of these compounds, their UV-vis absorption spectra

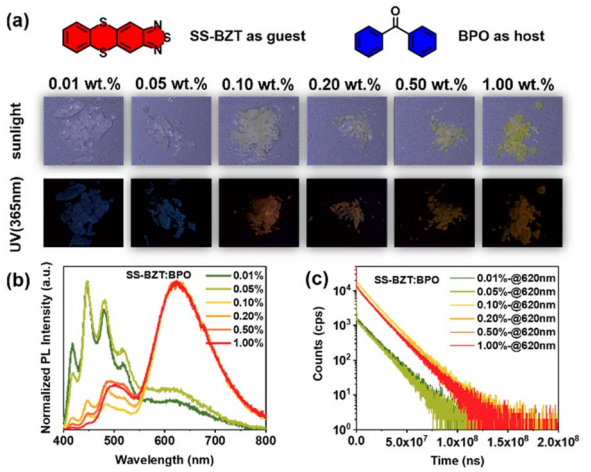

Fig. 2 (a) Images of SS-BZT : BPO doped crystals under sunlight and UV (365 nm) irradiation. (b) Normalized PL spectra of SS-BZT : BPO doped crystals. (c) Time-resolved PL spectra of SS-BZT : BPO doped crystals (monitored at 620 nm).

display almost the same main absorption bands in different diluted solutions (10^{-5} mol L^{-1}). Compared to parent chromophores (BZT, TA, PX, and DX), SS-BZT, SO-BZT, and OO-BZT all show a new red-shifted and broadened absorption band in the long-wavelength region. Taking TA, BZT, and SS-BZT in tetrahydrofuran (THF) solutions for example, both TA and SS-BZT exhibit the same absorption band peaking at 260 nm, which can be ascribed to the (π, π^*) transition characteristic. Differently, in contrast to TA and BZT, SS-BZT exhibits a broad absorption band peaking at 378 nm, which can be assigned to intramolecular charge-transfer (ICT) transition. For PL spectra, compared to their parent chromophores, SS-BZT, SO-BZT, and OO-BZT all show gradually red-shifted emission bands with increasing solvent polarity, indicating the presence of the ICT transition characteristic of the excited state. In detail, SS-BZT shows a significant redshift in the emission maximum, shifting from 465 nm in hexane (HEX) to 535 nm in acetonitrile (ACN), SO-BZT shows a shift from 430 nm in HEX to 505 nm in ACN, and OO-BZT shows a shift from 400 nm in HEX to 470 nm in ACN. As a matter of fact, BZT also shows a very weak ICT effect, which can be deduced from the slightly red-shifted emission maximum, shifting from 370 nm in HEX to 390 nm in ACN. According to the NTOs based on the optimized lowest excited singlet states (S_1) of SS-BZT, SO-BZT, and OO-BZT, it is observed that the holes are distributed over the folding moiety, while the electrons are localized on the BZT moiety, which can further confirm the presence of the ICT effect in these compounds (Fig. S16 and S17†). In the same solvent, the gradually red-shifted emission from OO-BZT and SO-BZT to SS-BZT can be rationalized by progressively enhancing the ICT properties, as a result of the larger atomic radius and electron density of the sulphur atom than those of the oxygen atom.

To differentiate between fluorescence and RTP, both PL spectra and time-resolved PL spectra were recorded for all the molecules in diluted THF solutions at RT and 77 K (Fig. 3a–c and S18–S21†), respectively. At RT, the PL spectra of TA, BZT, and SS-BZT exhibit a single emission band with a peak at 436 nm, 384 nm, and 515 nm, and time-resolved PL spectra present a nanosecond lifetime of 8.31 ns for TA (the lifetimes for BZT and SS-BZT are too short to be precisely calculated), which confirms their fluorescence emission characteristic. Once solutions were frozen at a temperature of 77 K, the PL spectra of TA, BZT, and SS-BZT all display two distinct emission bands located at 420 nm, 380 nm, and 470 nm in the short-wavelength region, together with 486 nm, 600 nm, and 620 nm in the long-wavelength region, respectively. Obviously, the short-wavelength emission is assigned to fluorescence, and the long-wavelength emission corresponds to phosphorescence with long lifetime [TA, 25.08 ms (19.28%) and 58.49 ms (80.72%); BZT, 19.97 ms (17.61%) and 33.64 ms (82.39%); SS-BZT, 17.07 ms (27.59%) and 23.57 ms (72.41%)] by the suppression of molecular thermal motions. The difference in the spectral maxima between fluorescence and phosphorescence for SS-BZT reaches 150 nm, basically inheriting that of the BZT chromophore (220 nm) and greatly improving that of TA (66 nm). Moreover, the phosphorescence emission of SS-BZT shows a remarkable bathochromic shift compared to BZT and TA. Apart from SS-BZT, both SO-BZT and OO-BZT also demonstrate obvious separation of spectral maxima between fluorescence and phosphorescence, as well as significantly red-shifted phosphorescence emission compared to the parent PX and DX, as shown in Table S2 and Fig. S18–S21.†

To further study the phosphorescence properties of these compounds in the single molecule doping state, PL spectra and time-resolved PL spectra for these compounds in 1.00 wt%-doped PMMA films were recorded under ambient/deoxygenated conditions and at RT/77 K, respectively (Fig. 3d–g and S22–S24†). Under ambient conditions, the PL spectra and time-resolved PL spectra of these studied compounds show a single fluorescence emission band with a short lifetime, which are similar to those in their solutions. After deoxygenation, they display new long-wavelength emission bands with a long-lived characteristic that can be attributed to the presence of RTP. For instance, under deoxygenated conditions, the SS-BZT-doped PMMA film exhibits two distinct emission bands peaking at 480 nm and 630 nm, and the time-resolved PL spectra show the lifetime monitored at 480 nm and 630 nm as 1.76 ns [0.45 ns (80.93%) and 2.69 ns (19.07%)] and 10.70 ms [7.48 ms (32.79%) and 11.70 ms (67.21%)], which can be assigned to fluorescence and RTP emission, respectively. Surprisingly, the spectral separation between fluorescence and RTP reaches 150 nm, and the RTP band is exactly located in the red region. The phosphorescence emission of the crystal of SS-BZT at 77 K exhibits a redshift when compared to its emission in the doping film state. This redshift may result from the molecular packing effect and intermolecular interactions. For comparison, the TA-doped film has an RTP emission with a peak at 520 nm in the green region, together with a blue fluorescence emission with a peak at 436 nm. As for BZT, the spectral separation between fluorescence (380 nm) and RTP (600 nm) emission maxima reaches 220 nm, which is much larger than those of TA and SS-BZT. Fluorescence quantum yields (Φ_Fs) of these doped films were measured to be 2.67% for SS-BZT, 3.6% for TA, and 0.43% for BZT, respectively, while Φ_Ps were estimated to be 1.73% for SS-BZT, 31.3% for TA, and 0.13% for BZT. As is well known, without significant heavy-atom effect (*e.g.*, metal and halogen), the efficient RTP of TA is mainly ascribed to the enhanced SOC with increasing folding degree of molecular geometry. In contrast, the Φ_P of SS-BZT is far lower than that of TA, which can be attributed to two aspects: one is that Φ_P is more limited by the energy-gap law for more red-shifted emission, and the other is the decreased SOC coefficient of SS-BZT relative to TA due to the smaller folding degree of SS-BZT than TA. Nevertheless, both SS-BZT and BZT are subject to the energy-gap law to a similar extent, as evidenced by their nearly identical red RTP emission, and therefore the enhanced RTP in SS-BZT compared to BZT can be ascribed to the introduction of the folding unit. In other words, the folding geometry plays a dominant role in enhancing the red RTP of SS-BZT. Consequently, the RTP efficiency of SS-BZT is significantly improved by more than ten times relative to that of BZT, the intrinsic mechanism of which will be rationalized in the following sections. In addition, the separation between fluorescence and RTP bands for SO-BZT and OO-BZT reaches 170 nm and 180 nm, respectively, which are also

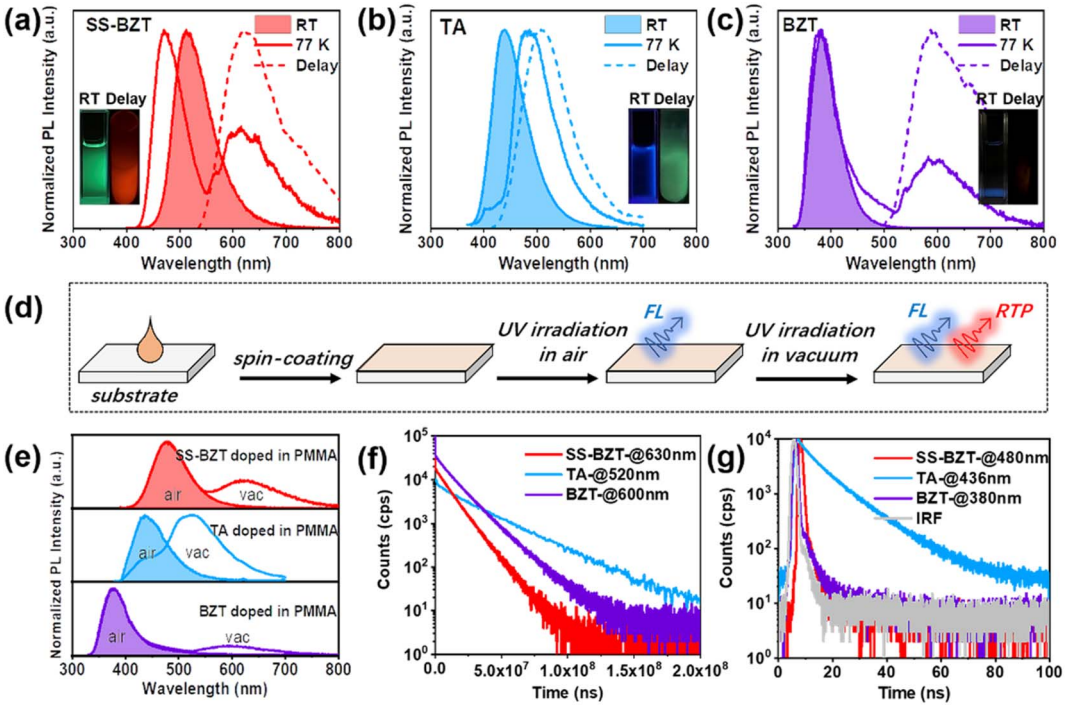

Fig. 3 PL spectra (conditions: RT and 77 K) and gated PL spectra (delay time: 1 ms) of (a) SS-BZT, (b) TA, and (c) BZT dispersed in THF solution at 10^{-5} mol L^{-1}. (d) Schematic of luminescence from doped PMMA film. (e) PL spectra of 1.00 wt% doped PMMA films for SS-BZT, TA, and BZT at RT (in air and vacuum). (f) and (g) Time-resolved PL spectra of 1.00 wt% doped PMMA films for SS-BZT, TA and BZT in a vacuum at RT.

obviously greater than those of PX and DX (Fig. S22†). The PL spectra of these doped films at 77 K also show two distinct emission bands that are similar to those of these compounds in diluted solutions at 77 K. The detailed data for SO-BZT, OO-BZT, and their parents (PX and DX) are summarized in Table 1.

Furthermore, in the case of the doped films incorporating these target compounds, their phosphorescence radiation rates (k_r^P) and ISC rates (k_{ISC}) were primarily estimated (Table S3†). Relative to SO-BZT and OO-BZT, the rate constants of SS-BZT are more representative when comparing them to TA and BZT. This comparison is convincing in revealing the underlying essence of improved photophysical properties achieved through the functional unit combination strategy in theory. Specifically, while the k_r^P and k_{ISC} values of SS-BZT are lower than those of TA, they still increase by one order of magnitude compared to BZT. This significant increase further supports the effectiveness of the mechanism in which the folded geometry induces the SOC enhancement. The detailed data for SO-BZT, OO-BZT, PX, and DX are shown in Table S3.†

Theoretical calculations

To elaborate the principle of the functional unit combination strategy, both density functional theory (DFT) and time-dependent density functional theory (TDDFT) calculations were performed on BZT and its derivatives. Their optimized geometries of S_0 and S_1 were obtained, together with NTOs of S_1 and the triplet states (T_n, $n = 1, 2$) (Fig. S16, S17 and S25–S30†). From the NTOs, the S_1 and T_2 states of SS-BZT, SO-BZT, and OO-

Table 1 Photophysical data of 1.00 wt% SS-BZT, TA, BZT, SO-BZT, PX, OO-BZT, and DX doped in PMMA films[a]

Molecule	λ_F (nm)	τ_F (ns)	λ_P (nm)	τ_P (ms)	Φ_F (%)	Φ_P (%)
SS-BZT	480	1.76 [0.45 (80.93%), 2.69 (19.07%)]	630	10.70 [7.48 (32.79%), 11.70 (67.21%)]	2.67	1.73
TA	436	11.41 [4.71 (33.12%), 12.65 (66.88%)]	520	23.36 [8.24 (14.59%), 24.24 (85.41%)]	3.60	31.3
BZT	384	3.13 [0.18 (96.98%), 5.97 (3.02%)]	600	14.17 [7.89 (25.83%), 15.30 (74.17%)]	0.43	0.13
SO-BZT	450	1.73 [0.49 (69.06%), 2.32 (30.94%)]	620	13.05 [8.50 (24.78%), 13.96 (75.22%)]	3.00	1.02
PX	375	11.65 [0.19 (94.96%), 14.48 (5.04%)]	475	9.85 [3.58 (46.11%), 15.21 (53.89%)]	0.20	1.20
OO-BZT	420	2.37 (100%)	600	18.76 (100%)	19.46	0.16
DX	371	1.58 [0.44 (69.69%), 2.12 (30.31%)]	—	—	0.60	—

[a] Here, λ_F and τ_F represent fluorescence emission wavelengths and their lifetimes monitored at fluorescence emission bands at RT; λ_P and τ_P represent RTP emission wavelengths and their lifetimes monitored at RTP emission bands in a vacuum at RT; Φ_F and Φ_P represent their PL efficiencies for fluorescence and phosphorescence emission, respectively.

BZT are characterized by their ICT properties, in which holes are localized on the folding moiety while electrons are mainly distributed over the BZT unit. Differently, their T_1 states are mainly dominated by the locally excited (LE) state, in which both holes and electrons are mainly located on the BZT unit. These results demonstrate that the phosphorescence of BZT derivatives should chiefly originate from the BZT unit. The slight redshift of the phosphorescence observed in these derivatives compared to parent BZT can be rationalized by the involvement of *n* lone pair electrons from sulphur and oxygen atoms in NTOs. Obviously, theoretical calculations show a clear trend of decreasing energy levels of S_1 states from OO-BZT to SO-BZT and finally to SS-BZT, due to the gradual increase in ICT strength in these derivatives. Interestingly, when it comes to the energy levels of T_1 states, all BZT derivatives exhibit nearly identical position. This can be attributed to the fact that they have almost the same LE state, which well accords with the results obtained from their photophysical measurements (Fig. S29†). Despite the fact that all BZT derivatives have T_1 states characterized by LE properties, both SS-BZT and SO-BZT show significantly enhanced RTP in comparison to parent BZT. To gain a deeper understanding of the distinct RTP properties, the SOC coefficients between S_1 and T_n (n = 1, 2) states were quantitatively estimated for BZT and its derivatives using the Beijing density function (BDF) program (Tables S4 and S5†).[78] Compared to BZT, SS-BZT and SO-BZT show obviously increased SOC coefficients between S_1 and T_n (n = 1, 2), meaning the greatly accelerated ISC process for SS-BZT and SO-BZT. On the other hand, the SOC coefficients of the S_1–T_1 and S_1–T_2 sequentially decrease from SS-BZT to SO-BZT and then to OO-BZT (Fig. 4a, S31d and S32d†), probably because of the diminishing participation of lone pair electrons from sulphur to oxygen atoms in the electron transition configurations, which occurs as the degree of folding gradually decreases. Apparently, these results demonstrate that the mechanism of folding-induced SOC enhancement plays a crucial role in efficient red RTP for SS-BZT. In essence, from BZT to SS-BZT and SO-BZT, the transition configurations of S_1 and T_n (n = 1, 2) undergo noticeable changes from (π, π^*) to a mixture of (n, π^*) and (π, π^*), which confirms that the lone pair electrons of sulphur atoms actively participate in the electron transition process. In comparison, OO-BZT always shows the (π, π^*) transition configurations for both S_1 and T_n (n = 1, 2) states. According to the El-Sayed rule,[79,80] the significant difference in electron transition configurations between singlet and triplet manifolds results in the amplification of SOC and, consequently, the substantial acceleration of the ISC process. This difference in electron transition configurations is the reason why SS-BZT and SO-BZT show more efficient red RTP than OO-BZT.

Notably, there is a gradual trend towards planarization in the molecular geometries from SS-BZT to SO-BZT and to OO-BZT in their S_0 states. Moreover, the geometries in their respective S_1 states become even more planar compared to those in the S_0 states (Fig. S30†). These changes in molecular geometry are very similar to those observed in the parent molecules TA and PX. The difference in SOC among these analogues may be ascribed to two main factors, including the heteroatom effect and folding dihedral angle. To evaluate the significance of these two factors, we further estimated the SOC coefficients of SS-BZT, SO-BZT, and OO-BZT with increasing folding dihedral angle from 100° to 180° at an interval of 10° (Fig. 4b, S31 and S32†). The occurrence of dominant photophysical and photochemical processes is related to S_1 and T_1 states according to Kasha's rule,[81] and thus we mainly calculated the SOC coefficient between S_1 and T_1 states. As the folding dihedral angle increases from 100° to 180°, the SOC coefficient of SS-BZT initially increases and then decreases. It reaches its peak value (9.019 cm^{-1}) at a folding dihedral angle of 110°, and this value

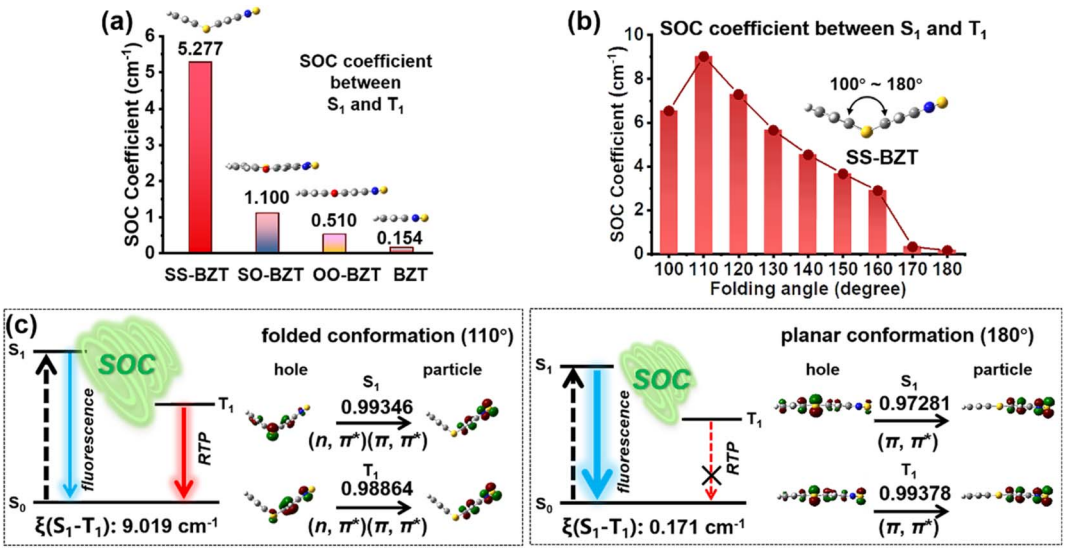

Fig. 4 (a) Molecular conformations and SOC coefficients for S_1–T_1 based on the molecular geometries of SS-BZT, SO-BZT, OO-BZT, and BZT in crystals. (b) SOC coefficients for S_1–T_1 based on the molecular geometries of the SS-BZT crystal at different folding dihedral angles. (c) Schematic of folding-induced SOC enhancement and NTOs of S_1 and T_1 states for SS-BZT in a folded conformation (110°) and planar conformation (180°).

is approximately one order of magnitude higher than the SOC coefficient of 0.171 cm^{-1} obtained when the molecule is entirely planar (with a folding dihedral angle is 180°) (Table S6†). While the folding dihedral angle is 180°, the SOC coefficients of S_1–T_1 for SS-BZT and BZT (0.154 cm^{-1}) are almost the same, which can verify that the folded configuration plays the dominant role in SOC enhancement compared to the heteroatom effect. The above results demonstrate that SS-BZT inherits the mechanism of folding-induced SOC enhancement from the TA unit, indicating the rationality of the functional unit combination strategy. Like SS-BZT, both SO-BZT and OO-BZT show a similar trend in the change of SOC coefficient as the folding dihedral angle increases (Table S6 and Fig. S31 and S32†). In addition, the SOC coefficients of S_1–T_2 also follow the mechanism of folding-induced SOC enhancement, indicating that the ISC process along high-lying excited states also works well for the role of folding conformation. Obviously, the nature of folding-induced SOC enhancement can be ascribed to the lone pair electrons of heteroatoms (S, O) becoming more protruded in the folded conformation compared to the planar conformation, which contributes to the purer (n, π^*) transition configuration (Fig. 4c and S33–S59†). As a whole, the more efficient red RTP is achieved in SS-BZT and SO-BZT than BZT using the functional unit combination strategy, in which the folded moiety and BZT moiety are responsible for SOC enhancement and red RTP emission, respectively.

Ratiometric oxygen sensing and detection

Purely organic RTP probes have emerged as outstanding candidates for optical oxygen sensing due to their ability to undergo non-radiative energy transfer from the excited triplet state of the probes to the ground triplet state of the analyte molecular oxygen. In order to detect oxygen concentration using a ratiometric method, it is beneficial to have a large spectral separation between fluorescence and phosphorescence.[82–85] Such ratiometric detection of oxygen concentration holds great significance in various fields such as physiology and pathology,[86,87] and food storage.[88] At first glance, BZT appears to be a promising candidate for ratiometric optical oxygen sensing and detection; however, there are certain drawbacks that make it less favourable for this application, such as weak RTP intensity and fluorescence emission in the UV region. Moreover, it has been observed that the PL intensities of both single crystals and doped crystals remain nearly unchanged when subjected to deoxygenation conditions, as compared to when they are in air. This case manifests that these crystals are not suitable candidates for oxygen sensing, as they exhibit poor oxygen permeability (Fig. S60 and S61†). In this work, by dispersing SS-BZT and SO-BZT in polymer films, a significant spectral separation between dual emission bands can be achieved to effectively remedy those drawbacks mentioned above. Taking 1.00 wt% SS-BZT dispersed in PMMA film for example (Fig. 5), the RTP emission band of the film was observed when the film was placed in a deoxygenated environment. However, this RTP emission band completely disappeared when the film was exposed to air. Obviously, oxygen concentration ($[O_2]$) of the mixed gas should be controlled to be sufficiently low, at least less than 21%, which is the normal atmospheric level of oxygen. After careful optimization, we finally chose the mixed gases within the hypoxia context ($[O_2]$ ranging from 0 to 1.31%). As the $[O_2]$ decreases, the PL spectra of the SS-BZT-doped film display a fluorescence emission peaking at 480 nm with almost constant intensity (it can act as an internal reference signal for oxygen sensing). Meanwhile, a new RTP emission band emerges at 630 nm, gradually strengthens, and reaches its maximum intensity at $[O_2] = 0$. To further quantify the oxygen-sensing performance, the ratio of RTP intensity (I_P) to fluorescence intensity (I_F) is defined as I and recorded as a function of $[O_2]$, which can be described by the Stern–Volmer equation (eqn (1)):[83,84]

$$\frac{I_0}{I} = \frac{\tau_0}{\tau} = 1 + K_{SV}[O_2] \quad (1)$$

where I_0 and I represent the ratios of PL intensity at $[O_2] = 0$ and a certain $[O_2]$, respectively; τ_0 and τ represent the lifetimes at $[O_2] = 0$ and a certain $[O_2]$, respectively, and lifetimes are detected at 630 nm; K_{SV} is the Stern–Volmer quenching constant.

A good linear relationship is fitted in the $[O_2]$ range of 0–1.31% (correlation coefficient is $R^2 = 0.996$ and the Pearson correlation coefficient is $r = 0.963$). K_{SV} is estimated as 2.66 kPa^{-1} and the quenching efficiency (Q) is 94.24% (Fig. 5b and c and S63†). For comparison, the SO-BZT doped PMMA film exhibits a fluorescence band peaking at 450 nm in the blue region and the RTP band peaking at 620 nm in the red region (Fig. S64†), and presents a linear relationship between I_0/I and $[O_2]$ ($R^2 = 0.998$, $r = 0.983$). Its K_{SV} and Q are estimated to be 3.63 kPa^{-1} and 95.46%, respectively. Furthermore, to verify the accuracy of detecting oxygen concentration, an additional standard sample with a known concentration of $[O_2] = 0.90\%$ was prepared, and then the PL signals were recorded for the SS-BZT- and SO-BZT-doped PMMA films (Fig. S65†). According to the linear relation between I_0/I and $[O_2]$, the calculated concentrations are 0.90% and 0.92% for the SS-BZT- and SO-BZT-doped PMMA film, respectively. The above experimental results demonstrate that both SS-BZT and SO-BZT doped PMMA films show promising potential as optical probes for ratiometric oxygen sensing and detection under hypoxic conditions.

To provide a more visually appealing colorimetric representation, luminescence images of the SS-BZT-doped PMMA film under 365 nm irradiation were captured at various $[O_2]$ (Fig. 5d), and their emission colors were then accurately characterized using Commission Internationale del'Eclairage (CIE) coordinates. With decreasing $[O_2]$, the emission color transitions from sky-blue, which is observed when the film is exposed to air, to off-white when $[O_2] = 0$. This transition can be represented by a linear change in the CIE coordinates, which shift from (0.161, 0.261) to (0.288, 0.293), as shown Fig. 5b. In contrast, the emission color of the SO-BZT-doped PMMA film transitions from blue to pink as the $[O_2]$ decreases (Fig. S64f†). Notably, the stability is also an extremely important factor that determines the application potential of the doped film for oxygen sensing and detection. For this purpose, the luminescence signals of SS-BZT- and SO-BZT-doped PMMA films were recorded by alternating between cyclic exposure to air and vacuum conditions

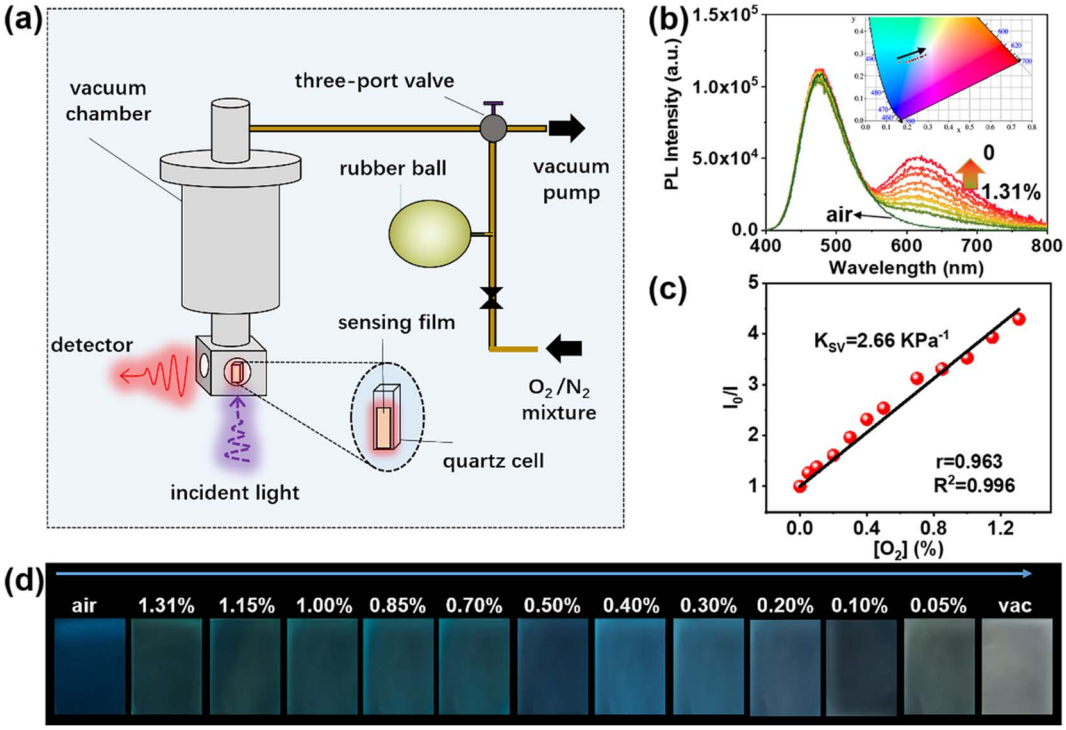

Fig. 5 (a) Schematic of detecting oxygen concentration in this work. (b) PL spectra and (c) plot of I_0/I against $[O_2]$ of 1.00 wt% SS-BZT-doped PMMA film at different $[O_2]$. Inset shows CIE coordinates corresponding to the PL spectra with decreasing $[O_2]$ of 1.00 wt% SS-BZT-doped PMMA film. (d) Images of 1.00 wt% SS-BZT-doped PMMA film under 365 nm irradiation with decreasing $[O_2]$.

(Fig. S66†). After several cycles, the intensity of all luminescence signals remained almost unchanged, indicating excellent stability for the practical application scenario.

Apart from polymeric matrix PMMA, Zeonex was also considered as the polymeric matrix because of its better oxygen permeability and rigidity.[89] Under deoxygenation condition, 1.00 wt% SS-BZT-doped Zeonex film exhibits two emission bands peaking at 465 nm and 620 nm, which are located in the blue and red regions, respectively (Fig. S67†). As the $[O_2]$ increases, the intensity of the RTP band in Zeonex film rapidly decreases, indicating a higher sensitivity compared to SS-BZT doped in PMMA film. This suggests that the SS-BZT-doped Zeonex film can be used as an oxygen probe, particularly in a hypoxic environment. When the $[O_2]$ reaches 0.20%, the RTP band is almost completely quenched, which can be attributed to the exceptional oxygen permeability of the Zeonex polymer matrix. The $K_{SV,\ intensity}$ value is estimated to be 17.54 kPa^{-1}, which is improved by about one order of magnitude relative to the SS-BZT-doped PMMA film. The detailed data are summarized in Fig. S67 and S68, and Table S7.†

Conclusions

In summary, we designed and synthesized a series of red RTP molecules (SS-BZT, SO-BZT, and OO-BZT) through a functional unit combination strategy, in which the folded units (TA and PX) were incorporated to enhance the SOC, while the BZT unit is mainly responsible for the red RTP emission. After deoxygenation, all three compounds in doped PMMA films exhibit dual emission with blue fluorescence and red RTP as we desired, but the OO-BZT-doped PMMA film shows extremely weak red RTP. Compared to OO-BZT and the parent BZT, both SS-BZT and SO-BZT demonstrate about one order of magnitude improvement in RTP efficiency. This improvement can be ascribed to the mechanism of folding-induced SOC enhancement for the folded geometries of SS-BZT and SO-BZT, which leads to increased generation of triplet excitons by accelerating the ISC process, while the planar OO-BZT exhibits weak SOC. In essence, the folded geometry induces the formation of an (n, π^*) transition configuration in the S_1 state, which facilitates the enhancement of SOC and thus the ISC process to increase the population of triplet excitons. Both experimental and theoretical investigations have provided validation for the new strategy of combining two functional units to achieve enhanced red RTP materials. Moreover, taking advantage of the large spectral separation between fluorescence and RTP, both SS-BZT and SO-BZT in the doped film were used as optical probes for ratiometric oxygen sensing and detection. Under hypoxic conditions (with $[O_2]$ ranging from 0 to 1.31%), the PL intensities in the doped film are used to estimate the K_{SV} for SS-BZT and SO-BZT as 2.66 and 3.63 kPa^{-1} respectively, indicating that SS-BZT and SO-BZT possess excellent detection accuracy and cycle stability as oxygen probes. The Zeonex polymer matrix with better oxygen permeability than PMMA further improves the K_{SV} of SS-BZT and SO-BZT. In other words, this work

provides a novel molecular design concept for efficient red RTP materials by a functional unit combination strategy, and also showcases the unique application of these materials in ratiometric optical oxygen sensing and detection.

Data availability

All necessary information is included in the ESI.†

Author contributions

Conceptualization: Z. Yang (Zhiqiang Yang), H. Liu, S.-T. Zhang, and B. Yang. Data curation: S. Zhao, Z. Yang (Zhiqiang Yang), X. Zhang, Y. Lv, S. Wang, and Z. Yang (Zhongzhao Yang). Chemical synthesis and product analysis: S. Zhao. DFT calculations: S. Zhao and Z. Yang (Zhiqiang Yang). Supervision: H. Liu and B. Yang. Funding acquisition: H. Liu and B. Yang. Writing – original draft: S. Zhao. Writing – review & editing: H. Liu and B. Yang.

Conflicts of interest

There are no conflicts to declare.

Acknowledgements

This work is supported by the National Natural Science Foundation of China (no. 52103209, 52073117, and 51873077) and the National Key Research and Development Program of China (no. 2020YFA0714603). Thanks to HZWTECH for providing computation facilities for this study.

Notes and references

1 Y. Ma, H. Zhang, J. Shen and C. Che, *Synth. Met.*, 1998, **94**, 245–248.
2 M. A. Baldo, D. F. O'Brien, Y. You, A. Shoustikov, S. Sibley, M. E. Thompson and S. R. Forrest, *Nature*, 1998, **395**, 151–154.
3 T. Wang, X. Su, X. Zhang, X. Nie, L. Huang, X. Zhang, X. Sun, Y. Luo and G. Zhang, *Adv. Mater.*, 2019, **31**, 1904273.
4 J. Wang, J. Liang, Y. Xu, B. Liang, J. Wei, C. Li, X. Mu, K. Ye and Y. Wang, *J. Phys. Chem. Lett.*, 2019, **10**, 5983–5988.
5 Z. Zhou, X. Xie, Z. Sun, X. Wang, Z. An and W. Huang, *J. Mater. Chem. C*, 2023, **11**, 3143–3161.
6 M. Li, W. Xie, X. Cai, X. Peng, K. Liu, Q. Gu, J. Zhou, W. Qiu, Z. Chen, Y. Gan and S.-J. Su, *Angew. Chem., Int. Ed.*, 2022, **61**, e202209343.
7 Y. Fan, S. Liu, M. Wu, L. Xiao, Y. Fan, M. Han, K. Chang, Y. Zhang, X. Zhen, Q. Li and Z. Li, *Adv. Mater.*, 2022, **34**, 2201280.
8 J. Yang, X. Zhen, B. Wang, X. Gao, Z. Ren, J. Wang, Y. Xie, J. Li, Q. Peng, K. Pu and Z. Li, *Nat. Commun.*, 2018, **9**, 840.
9 Y. Hou, G. Jiang, J. Gong, R. Sha and J. Wang, *Chem. Res. Chin. Univ.*, 2021, **37**, 73–82.
10 J. Yang, Y. Zhang, X. Wu, W. Dai, D. Chen, J. Shi, B. Tong, Q. Peng, H. Xie, Z. Cai, Y. Dong and X. Zhang, *Nat. Commun.*, 2021, **12**, 4883.
11 F. Xiao, H. Gao, Y. Lei, W. Dai, M. Liu, X. Zheng, Z. Cai, X. Huang, H. Wu and D. Ding, *Nat. Commun.*, 2022, **13**, 186.
12 C. Qian, Z. Ma, X. Fu, X. Zhang, Z. Li, H. Jin, M. Chen, H. Jiang, X. Jia and Z. Ma, *Adv. Mater.*, 2022, **34**, 2200544.
13 Z. Wang, A. Li, Z. Zhao, T. Zhu, Q. Zhang, Y. Zhang, Y. Tan and W. Z. Yuan, *Adv. Mater.*, 2022, **34**, 2202182.
14 S. Tang, Z. Zhao, J. Chen, T. Yang, Y. Wang, X. Chen, M. Lv and W. Z. Yuan, *Angew. Chem., Int. Ed.*, 2022, **61**, e202117368.
15 Y. Su, Y. Zhang, Z. Wang, W. Gao, P. Jia, D. Zhang, C. Yang, Y. Li and Y. Zhao, *Angew. Chem., Int. Ed.*, 2020, **59**, 9967–9971.
16 Z.-Y. Zhang and Y. Liu, *Chem. Sci.*, 2019, **10**, 7773–7778.
17 S. Hirata, *Appl. Phys. Rev.*, 2022, **9**, 011304.
18 S. Hirata, *Adv. Opt. Mater.*, 2017, **5**, 1700116.
19 G. Baryshnikov, B. Minaev and H. Ågren, *Chem. Rev.*, 2017, **117**, 6500–6537.
20 O. Bolton, K. Lee, H.-J. Kim, K. Y. Lin and J. Kim, *Nat. Chem.*, 2011, **3**, 205–210.
21 Z. Mao, Z. Yang, Y. Mu, Y. Zhang, Y.-F. Wang, Z. Chi, C.-C. Lo, S. Liu, A. Lien and J. Xu, *Angew. Chem., Int. Ed.*, 2015, **54**, 6270–6273.
22 S. Garain, S. Kuila, B. C. Garain, M. Kataria, A. Borah, S. K. Pati and S. J. George, *Angew. Chem., Int. Ed.*, 2021, **60**, 12323–12327.
23 D. R. Lee, K. H. Lee, W. Shao, C. L. Kim, J. Kim and J. Y. Lee, *Chem. Mater.*, 2020, **32**, 2583–2592.
24 X.-F. Wang, H. Xiao, P.-Z. Chen, Q.-Z. Yang, B. Chen, C.-H. Tung, Y.-Z. Chen and L.-Z. Wu, *J. Am. Chem. Soc.*, 2019, **141**, 5045–5050.
25 T. Weng, G. Baryshnikov, C. Deng, X. Li, B. Wu, H. Wu, H. Ågren, Q. Zou, T. Zeng and L. Zhu, *Small*, 2020, **16**, 1906475.
26 Z.-A. Yan and X. Ma, *ACS Mater. Lett.*, 2022, **4**, 2555–2561.
27 Z. Yang, Z. Fu, H. Liu, M. Wu, N. Li, K. Wang, S.-T. Zhang, B. Zou and B. Yang, *Chem. Sci.*, 2023, **14**, 2640–2645.
28 I. Bhattacharjee, N. Acharya, S. Karmakar and D. Ray, *J. Phys. Chem. C*, 2018, **122**, 21589–21597.
29 Z. Wang, X. Cheng, Y. Xie, S. Liu, M. Dong, J. Zhao, F. Liang, Z. An and W. Huang, *CCS Chem.*, 2023, **5**, 292–309.
30 M. Gao, Y. Tian, X. Li, Y. Gong, M. Fang, J. Yang and Z. Li, *Angew. Chem., Int. Ed.*, 2023, **62**, e202214908.
31 Y. Zhang, X. Chen, J. Xu, Q. Zhang, L. Gao, Z. Wang, L. Qu, K. Wang, Y. Li, Z. Cai, Y. Zhao and C. Yang, *J. Am. Chem. Soc.*, 2022, **144**, 6107–6117.
32 W. Zhao, Z. He, J. W. Y. Lam, Q. Peng, H. Ma, Z. Shuai, G. Bai, J. Hao and B. Z. Tang, *Chem*, 2016, **1**, 592–602.
33 S. Hirata and T. Kamatsuki, *J. Phys. Chem. C*, 2023, **127**, 3861–3871.
34 W. Shao and J. Kim, *Acc. Chem. Res.*, 2022, **55**, 1573–1585.
35 H. Liu, Y. Gao, J. Cao, T. Li, Y. Wen, Y. Ge, L. Zhang, G. Pan, T. Zhou and B. Yang, *Mater. Chem. Front.*, 2018, **2**, 1853–1858.

36 G. Pan, Z. Yang, H. Liu, Y. Wen, X. Zhang, Y. Shen, C. Zhou, S.-T. Zhang and B. Yang, *J. Phys. Chem. Lett.*, 2022, **13**, 1563–1570.
37 Y. Gong, L. Zhao, Q. Peng, D. Fan, W. Z. Yuan, Y. Zhang and B. Z. Tang, *Chem. Sci.*, 2015, **6**, 4438–4444.
38 W. Z. Yuan, X. Y. Shen, H. Zhao, J. W. Y. Lam, L. Tang, P. Lu, C. Wang, Y. Liu, Z. Wang, Q. Zheng, J. Z. Sun, Y. Ma and B. Z. Tang, *J. Phys. Chem. C*, 2010, **114**, 6090–6099.
39 Y. Wen, H. Liu, S. Zhang, Y. Gao, Y. Yan and B. Yang, *J. Mater. Chem. C*, 2019, **7**, 12502–12508.
40 J. Guo, C. Yang and Y. Zhao, *Acc. Chem. Res.*, 2022, **55**, 1160–1170.
41 J.-A. Li, L. Zhang, C. Wu, Z. Huang, S. Li, H. Zhang, Q. Yang, Z. Mao, S. Luo, C. Liu, G. Shi and B. Xu, *Angew. Chem., Int. Ed.*, 2023, **62**, e202217284.
42 Z. Wang, L. Gao, Y. Zheng, Y. Zhu, Y. Zhang, X. Zheng, C. Wang, Y. Li, Y. Zhao and C. Yang, *Angew. Chem., Int. Ed.*, 2022, **61**, e202203254.
43 T. Wang, J. De, S. Wu, A. K. Gupta and E. Zysman-Colman, *Angew. Chem., Int. Ed.*, 2022, **61**, e202206681.
44 Y. Zhang, Y. Su, H. Wu, Z. Wang, C. Wang, Y. Zheng, X. Zheng, L. Gao, Q. Zhou, Y. Yang, X. Chen, C. Yang and Y. Zhao, *J. Am. Chem. Soc.*, 2021, **143**, 13675–13685.
45 F. Lin, H. Wang, Y. Cao, R. Yu, G. Liang, H. Huang, Y. Mu, Z. Yang and Z. Chi, *Adv. Mater.*, 2022, **34**, 2108333.
46 F.-F. Shen, Z. Liu, H.-J. Yu, H. Wang, X. Xu and Y. Liu, Macrocyclic Confined, *Adv. Opt. Mater.*, 2022, **10**, 2200245.
47 D. Wang, Y. Xie, X. Wu, Y. Lei, Y. Zhou, Z. Cai, M. Liu, H. Wu, X. Huang and Y. Dong, *J. Phys. Chem. Lett.*, 2021, **12**, 1814–1821.
48 H.-J. Yu, Q. Zhou, X. Dai, F.-F. Shen, Y.-M. Zhang, X. Xu and Y. Liu, *J. Am. Chem. Soc.*, 2021, **143**, 13887–13894.
49 Y. Lei, W. Dai, Y. Tian, J. Yang, P. Li, J. Shi, B. Tong, Z. Cai and Y. Dong, *J. Phys. Chem. Lett.*, 2019, **10**, 6019–6025.
50 Y. Zhao, B. Ding, Z. Huang and X. Ma, *Chem. Sci.*, 2022, **13**, 8412–8416.
51 K. Fukasawa, Y. Sugawara, R. Tsuru, T. Yamashita and S. Hirata, *J. Phys. Chem. Lett.*, 2022, **13**, 7788–7796.
52 S. M. A. Fateminia, Z. Mao, S. Xu, Z. Yang, Z. Chi and B. Liu, *Angew. Chem., Int. Ed.*, 2017, **56**, 12160–12164.
53 B. Chen, W. Huang, X. Nie, F. Liao, H. Miao, X. Zhang and G. Zhang, *Angew. Chem., Int. Ed.*, 2021, **60**, 16970–16973.
54 W. Dai, Y. Zhang, X. Wu, S. Guo, J. Ma, J. Shi, B. Tong, Z. Cai, H. Xie and Y. Dong, *CCS Chem.*, 2022, **4**, 2550–2559.
55 S. Kuila, A. Ghorai, P. K. Samanta, R. B. K. Siram, S. K. Pati, K. S. Narayan and S. J. George, *Chem.–Eur. J.*, 2019, **25**, 16007–16011.
56 T. Ono, K. Kimura, M. Ihara, Y. Yamanaka, M. Sasaki, H. Mori and Y. Hisaeda, *Chem.–Eur. J.*, 2021, **27**, 9535–9541.
57 S. Sun, L. Ma, J. Wang, X. Ma and H. Tian, *Natl. Sci. Rev.*, 2022, **9**, nwab085.
58 T. Zhu, T. Yang, Q. Zhang and W. Z. Yuan, *Nat. Commun.*, 2022, **13**, 2658.
59 S. J. Jang, *J. Chem. Phys.*, 2021, **155**, 164106.
60 X. Chen, Z. Yang, W. Li, Z. Mao, J. Zhao, Y. Zhang, Y.-C. Wu, S. Jiao, Y. Liu and Z. Chi, *ACS Appl. Mater. Interfaces*, 2019, **11**, 39026–39034.
61 C. Wang, X. Li, Y. Pan, S. Zhang, L. Yao, Q. Bai, W. Li, P. Lu, B. Yang, S. Su and Y. Ma, *ACS Appl. Mater. Interfaces*, 2016, **8**, 3041–3049.
62 J. Liu, Z. Li, T. Hu, X. Wei, R. Wang, X. Hu, Y. Liu, Y. Yi, Y. Yamada-Takamura, Y. Wang and P. Wang, *Adv. Opt. Mater.*, 2019, **7**, 1801190.
63 L. Yao, S. Zhang, R. Wang, W. Li, F. Shen, B. Yang and Y. Ma, *Angew. Chem., Int. Ed.*, 2014, **53**, 2119–2123.
64 T. Liu, X. Chen, J. Zhao, W. Wei, Z. Mao, W. Wu, S. Jiao, Y. Liu, Z. Yang and Z. Chi, *Chem. Sci.*, 2021, **12**, 5171–5176.
65 Y. Zhang, J. Song, J. Qu, P.-C. Qian and W.-Y. Wong, *Sci. China: Chem.*, 2021, **64**, 341–357.
66 H. Shi, L. Zou, K. Huang, H. Wang, C. Sun, S. Wang, H. Ma, Y. He, J. Wang, H. Yu, W. Yao, Z. An, Q. Zhao and W. Huang, *ACS Appl. Mater. Interfaces*, 2019, **11**, 18103–18110.
67 G. He, L. Du, Y. Gong, Y. Liu, C. Yu, C. Wei and W. Z. Yuan, *ACS Omega*, 2019, **4**, 344–351.
68 G. D. Gutierrez, G. T. Sazama, T. Wu, M. A. Baldo and T. M. Swager, *J. Org. Chem.*, 2016, **81**, 4789–4796.
69 T. Ishi-i, R. Kichise, I. S. Park, T. Yasuda and T. Matsumoto, *J. Mater. Chem. C*, 2023, **11**, 3003–3009.
70 B. Ding, H. Gao, C. Wang and X. Ma, *Chem. Commun.*, 2021, **57**, 3154–3157.
71 Y. Wen, H. Liu, S.-T. Zhang, G. Pan, Z. Yang, T. Lu, B. Li, J. Cao and B. Yang, *CCS Chem.*, 2021, **3**, 1940–1948.
72 Z. Yang, S. Zhao, X. Zhang, M. Liu, H. Liu and B. Yang, *Front. Chem.*, 2022, **9**, 810304.
73 J. Yuan, Y. Song, X. Li, J. Xie, S. Dong and K. Zhu, *Org. Lett.*, 2021, **23**, 9554–9558.
74 S. Wang, J. Yuan, J. Xie, Z. Lu, L. Jiang, Y. Mu, Y. Huo, Y. Tsuchido and K. Zhu, *Angew. Chem., Int. Ed.*, 2021, **60**, 18443–18447.
75 H. Liu, G. Pan, Z. Yang, Y. Wen, X. Zhang, S.-T. Zhang, W. Li and B. Yang, *Adv. Opt. Mater.*, 2022, **10**, 2102814.
76 Y. Chen, Y. Xie, H. Shen, Y. Lei, Y. Zhou, W. Dai, Z. Cai, M. Liu, X. Huang and H. Wu, *Chem.–Eur. J.*, 2020, **26**, 17376–17380.
77 G. Zhang, G. M. Palmer, M. W. Dewhirst and C. L. Fraser, *Nat. Mater.*, 2009, **8**, 747–751.
78 W. Liu, F. Wang and L. Li, *J. Theor. Comput. Chem.*, 2003, **02**, 257–272.
79 M. A. El-Sayed, *J. Chem. Phys.*, 1963, **38**, 2834–2838.
80 M. A. El-Sayed, *J. Chem. Phys.*, 1963, **38**, 3032–3033.
81 M. Kasha, *Discuss. Faraday Soc.*, 1950, **9**, 14–19.
82 K. Leitonas, A. Tomkeviciene, G. Baratte, A. Dabuliene, S. M. Punniyakoti, D. Volyniuk and J. V. Grazulevicius, *Sens. Actuators, B*, 2021, **345**, 130369.
83 Y. Feng, J. Cheng, L. Zhou, X. Zhou and H. Xiang, *Analyst*, 2012, **137**, 4885–4901.
84 X.-D. Wang and O. S. Wolfbeis, *Chem. Soc. Rev.*, 2014, **43**, 3666–3761.
85 Y. Yu, M. S. Kwon, J. Jung, Y. Zeng, M. Kim, K. Chung, J. Gierschner, J. H. Youk, S. M. Borisov and J. Kim, *Angew. Chem., Int. Ed.*, 2017, **56**, 16207–16211.
86 G. Zhang, G. M. Palmer, M. W. Dewhirst and C. L. Fraser, *Nat. Mater.*, 2009, **8**, 747–751.

87 A. V. Zhdanov, I. A. Okkelman, A. V. Golubeva, B. Doerr, N. P. Hyland, S. Melgar, F. Shanahan, J. F. Cryan and D. B. Papkovsky, *Cell. Mol. Life Sci.*, 2017, **74**, 141–151.
88 F. C. O'Mahony, T. C. O'Riordan, N. Papkovskaia, V. I. Ogurtsov, J. P. Kerry and D. B. Papkovsky, *Packag. Technol. Sci.*, 2004, **17**, 225–234.
89 L. Skhirtladze, K. Leitonas, A. Bucinskas, K. L. Woon, D. Volyniuk, R. Keruckienė, M. Mahmoudi, M. Lapkowski, A. Ariffin and J. V. Grazulevicius, *Sens. Actuators, B*, 2023, **380**, 133295.